

A synthetic diagnostic for validation of electron gyroradius scale turbulence simulations against coherent scattering measurements

F. M. Poli,^{1,a)} S. Ethier,² W. Wang,² T. S. Hahm,² E. Mazzucato,² and D. R. Smith³

¹University of Warwick, Gibbet Hill road, Coventry CV4 7AL, United Kingdom

²Princeton Plasma Physics Laboratory, Princeton, New Jersey 08543, USA

³Department of Engineering Physics, University of Wisconsin-Madison, Wisconsin, USA

(Received 28 June 2010; accepted 2 September 2010; published online 24 November 2010)

Comparison between spectra of short-scale density fluctuations measured with coherent electromagnetic scattering experiments and those extracted from space-resolved numerical simulations is affected by a number of systematic errors. These include the locality of scattering measurements, the different domain covered (space-resolved simulations versus wavenumber resolved measurements), and the stationarity of simulated nonlinear spectra. To bridge the gap between theory-simulations and experiments, a synthetic diagnostic for high- k scattering measurements has been developed. This synthetic scattering predicts the propagation of the beam in an anisotropic, inhomogeneous plasma and accounts for the spatial variation of the instrumental transfer function. The latter, in particular, is proven to provide an important calibration factor not only for the simulated spectra, but also for the measured ones, allowing the use of the synthetic diagnostic in predictive mode. Results from a case study for National Spherical Torus Experiment plasmas using high- k tangential scattering system [Smith *et al.*, Rev. Sci. Instrum. **75**, 3840 (2004)] and the gyrokinetic tokamak simulation code [Wang *et al.*, Phys. Plasmas **13**, 092505 (2006)] are presented. © 2010 American Institute of Physics. [doi:10.1063/1.3492715]

I. INTRODUCTION

Microturbulence can cause anomalous transport in magnetically confined plasmas. For instance, fluctuations with perpendicular wavelengths at the ion gyroradius scale, such as ion temperature gradient driven instabilities and trapped electron modes, can lead to anomalous level of both ion and electron heat transport. Interestingly, the National Spherical Torus Experiment¹ (NSTX) exhibits examples in which those low- k instabilities at ion gyroradius scale are predicted to be stable, when the stabilizing effects of mean $\mathbf{E} \times \mathbf{B}$ shear are properly taken into account.²⁻⁴ Since ion thermal transport in those plasmas was near to neoclassical levels, while electron thermal transport remain highly anomalous, shorter scale instabilities in the range of electron gyroradius (ETG), which are less affected by large scale mean $\mathbf{E} \times \mathbf{B}$ and contribute mainly to electron thermal transport, were considered as a strong candidate.

In response to a need for resolving the paradigm of transport in tokamaks and motivated by the predictions of numerical turbulence simulations with increasing level of sophistication, a number of new diagnostics for turbulence measurements have been developed to characterize the correlation length and spectral amplitude of fluctuations over a wide range of spatial scales, spanning from the system size down to dissipation scales at the electron gyroradius.⁵⁻⁹

Recent experiments on NSTX, based on coherent scattering of electromagnetic waves, have revealed the presence of short-scale density fluctuations, whose spectra peak at frequencies and wavenumbers that are consistent with ETG instabilities.¹⁰⁻¹³ It was found that the power spectrum of

fluctuations follows a power law ($\sim k_{\perp}^{-4.5}$) dependence both in the case of inboard and outboard measurements despite of the electron temperature being three times higher in the former case.¹¹ A first comparison with nonlinear ETG simulations has been attempted in the case of the gyrokinetic tokamak simulation (GTS) code, a global code, run in realistic tokamak configuration.¹⁴ Measured and simulated spectra are qualitatively similar, both showing a power scaling law, although the simulated spectra appear to be less steep than the measured ones.^{11,15}

To bridge the gap between theory-simulations and experiments a *synthetic diagnostic* for high- k scattering measurements has been developed and tested on the GTS simulations for a plasma case study on NSTX. In order to decrease discrepancies between models and experiments, to disentangle fortuitous agreement, to differentiate between different models, and also in response to principles and best practices urged by the U.S. Transport Task Force Working Group on Verification and Validation,^{16,17} synthetic diagnostics are playing an increasingly important role in turbulence validation.^{18,19,16,17} Reproducing the instrumental spatial and temporal transfer function, they mimic the characteristics of measurements, reproducing the diagnostic uncertainties arising from sensitivities and resolution limitations, and replicate plasma modeling inherent in signal interpretation.

In this work we discuss the systematic errors that occur in the comparison between density fluctuations measured with a scattering diagnostic (resolved in the wavenumber domain) and those generated by nonlinear simulation (resolved in the spatio-temporal domain) and present a model that eliminates the major sources of uncertainties that may lead to a fortuitous agreement. The paper is organized as

^{a)}Electronic mail: fpoli@pppl.gov.

follows. Section II summarizes the principles of coherent scattering of electromagnetic waves in anisotropic plasmas and discusses measured and simulated fluctuations, as well as the issues related to theory-experiment comparison. Based on the expression of the measured, scattered electric field, the structure of the synthetic diagnostic is illustrated in Sec. III. Sources of uncertainties and systematic errors in the computation of the synthetic spectra are discussed in Sec. IV, while the implications of these results for theory-experiment comparison are discussed in Sec. V.

II. MEASURED AND SIMULATED DENSITY FLUCTUATIONS

Coherent scattering of high frequency electromagnetic waves is a powerful technique for detection of short-scale density perturbations.^{6,20} The frequency and wavenumber (\mathbf{k}, ω) of fluctuations must satisfy the conservation of energy and momentum

$$\omega = \omega_s - \omega_i \quad \mathbf{k} = \mathbf{k}_s - \mathbf{k}_i, \quad (1)$$

where subscripts i and s refer to the incident and scattered wave. Under the experimental conditions on NSTX, where $\omega_i/2\pi=280$ GHz and drift wave fluctuations have frequencies typically below a few megahertz, we have $\omega_s \approx \omega_i$ and $k_s \approx k_i$. The scattering angle θ_s must therefore satisfy the Bragg condition

$$k \approx 2k_i \sin(\theta_s/2). \quad (2)$$

For a Gaussian beam with waist a , the wavenumber resolution of measured fluctuations depends on the beam spectrum $G(\kappa_\perp) = \exp(-\kappa_\perp^2/\Delta^2)$, where $\Delta=2/a$ and κ_\perp is the wavenumber perpendicular to the direction of propagation (which is distinct from k_\perp , the wavenumber perpendicular to the magnetic field). In tokamaks, where turbulence is highly anisotropic and fluctuations have a small component along the magnetic field, the collection efficiency and the spatial resolution are affected by the geometry of injection because small variations in the magnetic field direction can detune the scattering receiver.^{6,20} The collection efficiency is optimized when the wave front of the incident beam coincides with the plane of propagation of fluctuations.

In addition to the spatial variation in the magnetic field pitch angle, the collection efficiency also depends on the mismatch in the scattering angle. If the receiving antenna is positioned for collecting with maximum efficiency the waves scattered from a given point, with angle θ_0 , those scattered from a second point will be collected with a relative efficiency that depends on $\Delta\theta=\theta-\theta_0$. The efficiency will strongly decrease for incidence angles outside the viewing angle of the receiving antenna. For small scattering angles and for oblique propagation, a condition that is satisfied in the present experimental setup, and using $k_s \approx k_i$, the instrumental selectivity function can be derived replacing $\kappa_\perp \approx k_i \alpha$, where α is the angle between the wave vector aligned with the center of the detecting antenna and a generic wave vector scattered at a different position

$$\cos \alpha = \cos(\theta - \theta_0) - 2 \sin \theta_0 \sin \theta \sin^2(\delta\phi/2). \quad (3)$$

The full derivation can be found in Refs. 6 and 21. Equation (3) explicitly contains two contributions: the difference in scattering angle ($\theta - \theta_0$) and the spatial variation in the magnetic field pitch angle $\delta\phi$. This relation is valid in general for oblique propagation and for fluctuations with all possible wavenumbers scattered at different locations along the probe beam. It will be used to reconstruct the profile of (k_r, k_θ) measured at the location of the detecting antennas, as discussed in Sec. III B.

A. Measured density fluctuations

On NSTX, fluctuations with wavenumbers in the range of 5–20 cm^{-1} can be detected injecting a microwave beam, with frequency of 280 GHz, tangentially to the magnetic field, with an inclination of 5° below the equatorial plane.^{22–24} The beam is collimated before entering the vessel and it can be directed to different plasma radii, through a translatable, rotatable mirror, with scattered radiation collected at both positive and negative scattering angles, over a 20° range. With this geometry, the scattering region can be positioned to measure the core (inboard launch configuration) or the edge (outboard launch configuration) fluctuations. The geometry of injection and detection for the experiments considered in this work is sketched in Fig. 1.

The probe and scattered waves lie nearly on the equatorial plane, so that the wave vectors of detected fluctuations are mainly perpendicular to magnetic surfaces, with a radial component about four times larger than the poloidal component. Five detection antennas measure density fluctuations associated with perpendicular wavenumbers in the range $(k_\perp \pm dk_\perp)$, where k_\perp is determined by solving ray tracing equations and dk_\perp depends on the beam waist and on the detection geometry, as it will be discussed in Sec. III B. By simultaneously adjusting the launch and collection mirror angles, the system can be used to fill in the wavenumber gaps between channels on a shot-to-shot basis.

The in-phase $I(t)$ and quadrature $Q(t)$ components of the signal are digitized at 7.5 MHz, with density fluctuations in the form

$$\tilde{n}_{HK}(\mathbf{k}, t) = I(t) + iQ(t) = A(t)e^{i\varphi(t)}, \quad (4)$$

where $A(t)$ and $\varphi(t)$ represent possible modulation of a pure carrier wave $\sin(2\pi ft)$. Combining measurements at different scattering angles (i.e., associated with different values of \mathbf{k}_\perp) the spectral index β can be extracted from a discrete representation of the wavenumber spectrum $P(k_\perp) \propto k_\perp^{-\beta}$. An example is shown in Fig. 2, for a NSTX He plasma, with $B_T=5.5$ kG, $I_p=600$ kA, heated by 2 MW of radio-frequency power, and reversed q profile ($q_0 - q_{\min}=0.8$). At 300 ms the electron density and temperature peaking values are, respectively, $n_e=1.4 \times 10^{13} \text{ cm}^{-3}$ and $T_e=3.3$ keV. The wavenumber spectrum follows a power law $\propto k_\perp^{-\beta}$, with $\beta=(4.23 \pm 0.08)$, a value close to what already found for similar plasmas.¹¹ The spectra have been computed during a time window of 10 ms, centered about 0.3 s. The frequency spectrum associated with $k_\perp \approx 11 \text{ cm}^{-1}$ is shown in Fig. 2(a). The large spike measured at zero frequency, the so-called

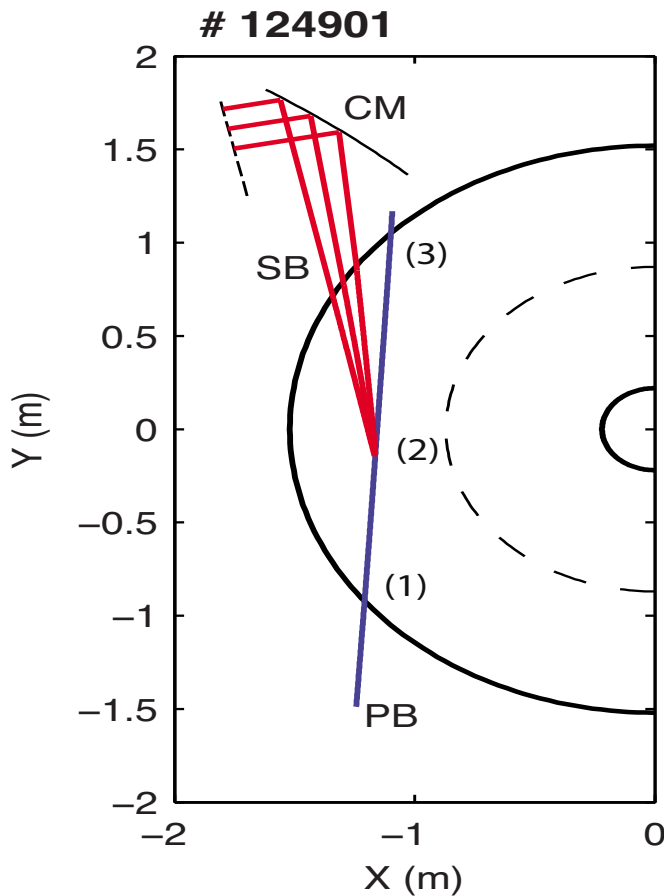


FIG. 1. (Color online) Sketch of the torus from the top, showing the geometry of injection and the collection mirror (CM) for measurement of inboard fluctuations for the case considered. Scattered beam (SB) and probe beam (PB) are indicated. Numbers along the probe beam indicate the position at which the wave fronts shown in Fig. 6 have been computed.

stray light, is due to multiple reflections and it is an unavoidable contribution present in optical systems. The measured frequency spectra are broad and asymmetric, with turbulent fluctuations propagating along the electron diamagnetic direction, which, in this work, corresponds to positive frequencies.

B. Simulated density fluctuations

Nonlinear, global simulations have been run with the GTS code in realistic tokamak geometry, for input background profiles at time $t=0.3$ s, over an annulus of plasma approximately $400\rho_e \approx 7$ cm wide (measured at midplane), centered at $r/a \approx 0.3$ ($\psi=0.265$), in the region covered by the high- k scattering measurements (see Fig. 3). Overall parametric dependence of onset condition for ETG instabilities can be found in the work by Jenko *et al.*,²⁵ who summarized results from many linear simulation results in terms of previous analytic formulas.^{26,27} GTS nonlinear simulations show that ETG turbulence level and associated electron transport are also very sensitive to the values of Z_{eff} and magnetic shear.

The evolution of electrostatic potential and density perturbations is evolved from the linear phase throughout the nonlinear saturated phase for 10^4 time steps, for a total of

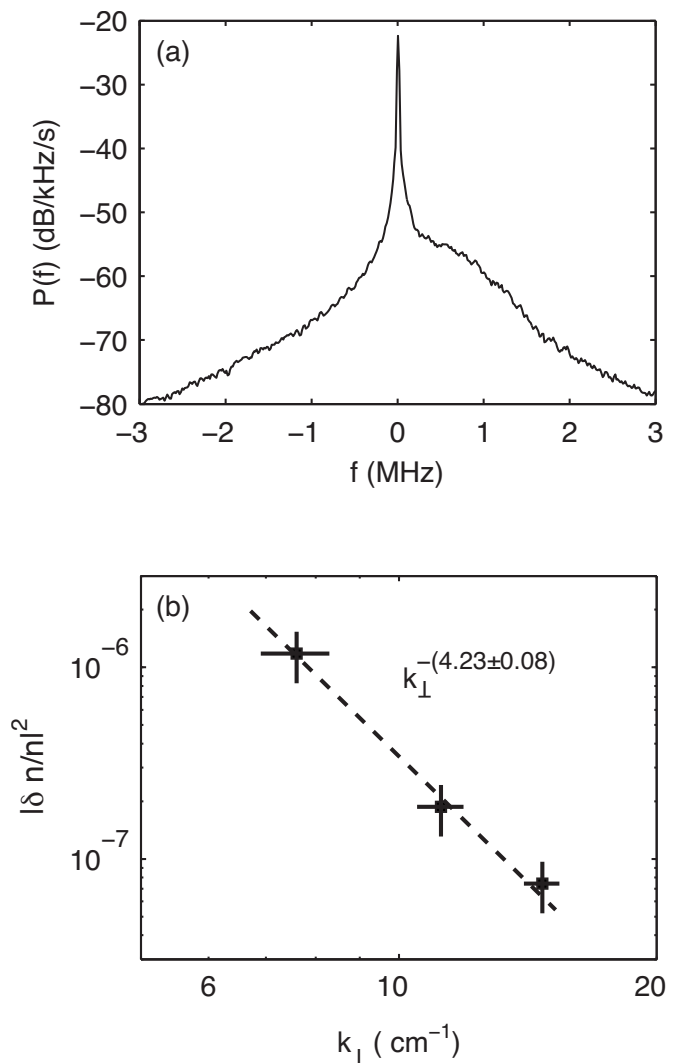


FIG. 2. (a) Frequency spectrum associated with fluctuations at $k_{\perp} = 11$ cm^{-1} , averaged during a time window of 10 ms, centered at 0.3 s. (b) Wavenumber spectrum, averaged during the same time window and integrated over frequencies.

22 μs , on each poloidal plane along a field-line-following mesh.¹⁴ Along the poloidal direction $\Delta\theta(r)$ is uniform on a flux surface in magnetic coordinates, while it varies over different flux surfaces. The separation between flux surfaces and the value of $\Delta\theta(r)$ is such that, when measured in real coordinates and at midplane, it is correlated with the local electron gyroradius.¹⁴

A three-dimensional view of density fluctuations during the nonlinear phase is shown in Fig. 4, together with the mean squared value, averaged over each flux surface. For this particular set of equilibrium profiles, fluctuation intensity is highest at two radial locations. Most nonlinear gyrokinetic simulations reported that ETG turbulence develops into a nonlinearly saturated state dominated by radially elongated eddies, called *streamers*, visible in Fig. 4 at $R \approx 1.2$ m. These streamers are expected to enhance the electron heat diffusivity^{25,28} of plasmas beyond the mixing length estimate based gyroBohm level, on the order of $(\rho_e/a)(cT_e/eB)$, which is too low to be experimentally relevant, while the enhancement factor varies significantly de-

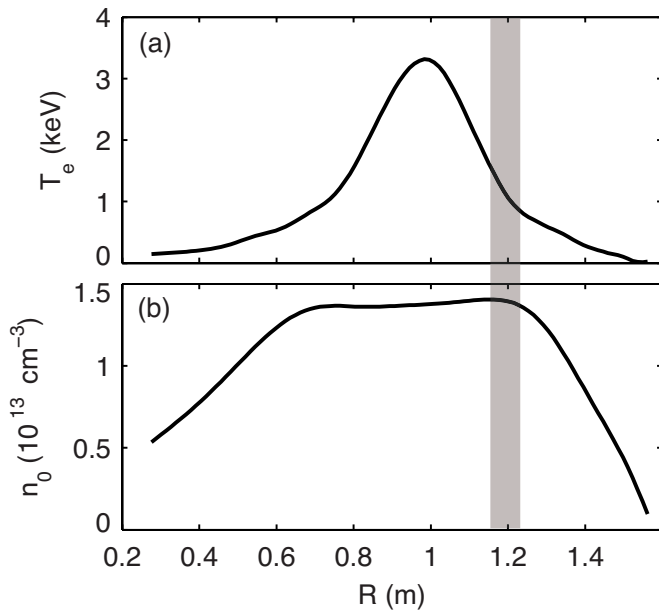


FIG. 3. (Color online) Electron temperature (a) and density (b) profile, measured at $t=0.3$ s with a Thomson scattering diagnostic and used as input for the GTS simulations. The shaded stripe indicates the plasma region covered by the simulation.

pending on simulation methods and the case studied.^{29–32}

Simulations are carried out over time steps $\delta t = 0.1 L_T / v_{th}$, where $L_T = |\nabla \ln T_e|^{-1}$ is the electron temperature gradient scale length and $v_{th} = \sqrt{T_e / m_e}$ is the electron thermal velocity. For the case under study the time resolution is $\delta t = 2.19 \times 10^{-9}$ s, although for computational efficiency the numerical output is stored every ten time steps, which correspond to a sampling rate of about 46 MHz, still six times higher than in the experiments. The decimation of data could in principle cause aliasing of those components with frequencies higher than $(10\delta t)^{-1}$. In practice this is not an issue in the case of drift-wave fluctuations, whose typical frequencies are well below the ion cyclotron frequency, which is about 26 MHz for the helium plasma considered in the present experiment. The frequency distribution of normalized density fluctuations, calculated at midplane using the nominal time resolution δt , is shown in Fig. 5, for two different radial locations: at $R \sim 1.2$ m, where fluctuations peak, and at $R \sim 1.23$ m. Spectral components of interest have frequencies below 10^{-2} of the Nyquist frequency and the drop in amplitude with respect to the peaking value is about 10^{-2} at 23 MHz.

C. Possible approaches to a comparison and sources of uncertainties

Comparison between theory and measurements should be done in the (\mathbf{k}, ω) domain, combining the information on the maximum spectral amplitude in wavenumber and frequency space and the spectral index extracted from the time or frequency averaged wavenumber spectra $P(\mathbf{k}_\perp)$. Wavenumber spectra from simulations have an advantage of spanning almost three orders of magnitude in \mathbf{k} . Provided simulations are run for a time sufficiently long to reach nonlinear saturation, statistically robust fluctuation spectra can be

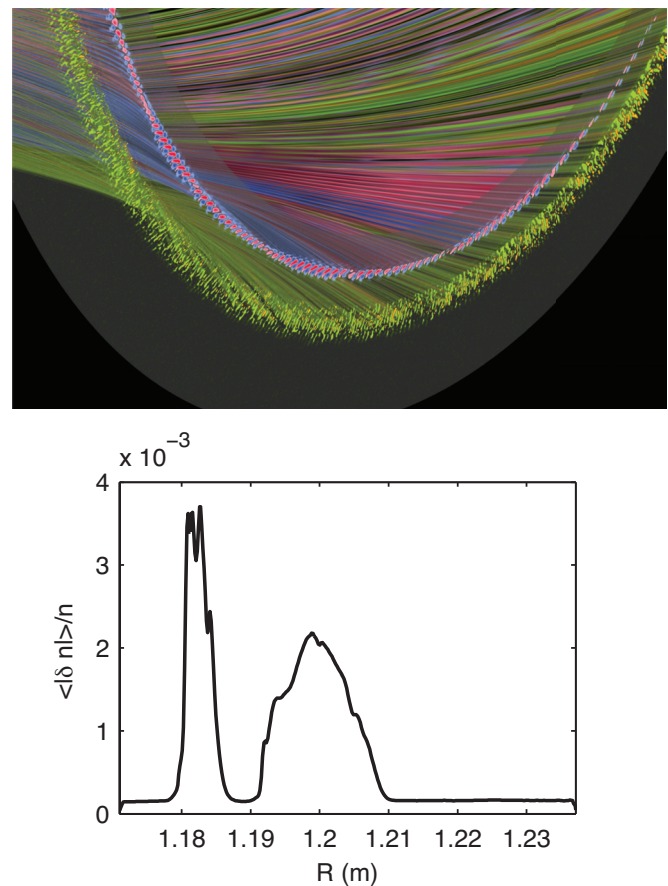


FIG. 4. (Color) (a) Three dimensional view of density fluctuations, computed with the GTS code, in an annulus of plasma $400\rho_e$ wide, during the nonlinear phase, showing the presence of radially elongated streamers [by Kwan-Liu Ma, Chad Jones, and Chris Ho, UC Davis, as part of the SciDAC Ultrascale Visualization Institute]. (b) Mean squared value of density fluctuations, computed over each flux surface and for $R > R_0$, normalized to the average density.

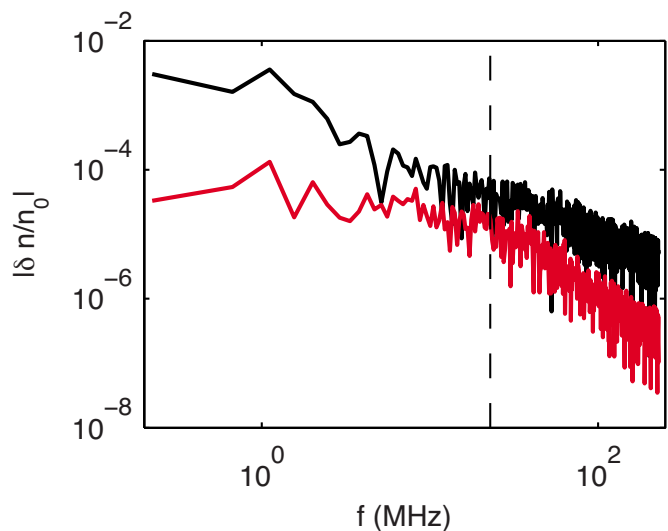


FIG. 5. (Color online) Frequency spectra, computed at midplane at $R=1.2$ m (black) and at $R=1.23$ m, over 600 time steps, using the nominal time resolution $\delta t=2 \times 10^{-9}$ s. The vertical line indicates the Nyquist frequency associated with the time series decimated by a factor of 10.

found. The full $(k_r, k_\theta, k_\phi, \omega)$ spectrum can be reconstructed and the perpendicular wavenumber can be calculated from the individual components across the magnetic field. Conversely, a scattering diagnostic measures density fluctuations associated with discrete values of the perpendicular wavenumber. Only a few points are available during a plasma discharge, although gaps in the measured \mathbf{k}_\perp can be filled by adjusting the direction of injection and detection. The radial and poloidal components of wavenumber are identified from the geometry of scattering using ray tracing equations and the reconstructed magnetic equilibrium. Systematic errors may come from uncertainties in the measured background density profile, or from imperfect mapping of magnetic topology to laboratory coordinates, from restrictions on equilibrium specification and its modeling. These same errors likely affect both experiments and models, since the same plasma profiles and magnetic equilibrium are used as an input to run the JSOLVER equilibrium solver³³ to get a high-resolution equilibrium reconstruction.

A first attempt of comparison between the spectra $P(k_\perp)$ measured at normalized radius $r/a=0.3$ and the simulated spectra at midplane $P(k_r)$ has recently been done.¹¹ Although a qualitative agreement was found, with both spectra following a power law dependence, this comparison is not conclusive. For each value of k_\perp that satisfies the Bragg's condition (2), only a limited range of (k_r, k_θ) satisfy the momentum conservation Eq. (1). These values should be selected from the simulated spectrum for a meaningful comparison and filtered through the response function of the high- k scattering diagnostic.

A comparison based on the frequency spectra is more straightforward because peaks in the simulated spectra, either in the (k_r, k_θ, ω) or in the (k_\perp, ω) domain, can be contrasted to peaks in the frequency spectra measured at the receiving positions. A limitation might be represented by the total duration of simulations, which should be long enough to resolve significant spectral components at the lowest frequencies in the measured spectrum.

III. STRUCTURE OF THE SYNTHETIC DIAGNOSTIC

The ingredients needed to a synthetic diagnostic for coherent scattering experiments can be obtained from the expression of the retarded field, scattered from a single particle in the dipole approximation.³⁴ For a monochromatic, incident wave

$$\mathbf{E}_i(\mathbf{r}, t) = \mathbf{E}_i(\mathbf{r})e^{i(\mathbf{k}_i \cdot \mathbf{r} - \omega t)} \quad (5)$$

and using the conservation of energy and momentum (1), the frequency spectrum of the field scattered during a finite time interval T (at distance x), integrated over the particle distribution function, is given by³⁴

$$\mathbf{E}_s(\nu_s) = \frac{r_e}{x} e^{ik_s x} \Pi \cdot \int_T dt' \int_V d^3 r' \mathbf{E}_i(\mathbf{r}') e^{i(\omega t' - \mathbf{k} \cdot \mathbf{r}')} \tilde{n}(\mathbf{r}', t'), \quad (6)$$

where $\Pi = \hat{\mathbf{s}} \times \hat{\mathbf{s}} \times \equiv \hat{\mathbf{s}}\hat{\mathbf{s}} - \mathbf{1}$ in the dipole approximation,³⁴ r_e is the classic radius of an electron, and $\hat{\mathbf{s}}$ identifies the direction

of scattering. This integral represents the Fourier transform of density fluctuations over the scattering volume V and during the scattering time T , weighted by the intensity profile $\mathbf{E}_i(\mathbf{r})$ of the beam.

Equation (6) identifies three separate contributions in the synthetic high- k scattering: the computation of wavenumber and frequency spectra from space and time resolved density fluctuations, the characterization of the scattering volume (position and extension), and the identification of the measured fluctuation wavenumbers from the scattering geometry. The three parts are separately described below, starting from the ray tracing equations, which represent a central part of the synthetic high- k scattering, because they provide the information needed for the computation and the calibration of spectra from the instrumental selectivity function.

A. Ray tracing

The electric field (5), solution of the wave equation, can be written as³⁵

$$\mathbf{E} = \mathbf{E}_0 e^{i(k_0 S - \omega t)}, \quad (7)$$

where k_0 is the wavenumber in vacuum, \mathbf{E}_0 is a slowly varying function of space and $S = R + iI$ is the *complex eikonal function*, which, in the quasioptical approximation, leads to the complex eikonal equation

$$(\nabla S)^2 = N^2, \quad (8)$$

where $N = N(\mathbf{x}, \mathbf{k}', \omega)$ is the refractive index of the anisotropic and inhomogeneous plasma. The propagation of the beam, initially Gaussian with waist a , is followed by solving the ray tracing equations³⁶

$$\frac{d\mathbf{x}}{dt} = - \frac{\partial D / \partial \mathbf{k}'}{\partial D / \partial \omega} = \mathbf{v}_g, \quad (9a)$$

$$\frac{d\mathbf{k}'}{dt} = \frac{\partial D / \partial \mathbf{x}}{\partial D / \partial \omega}. \quad (9b)$$

The dispersion relation $D(\mathbf{x}, \mathbf{k}', \omega)$ is associated with the real part of the eikonal equation and, defining $\mathbf{k} = \mathbf{k}' + i\mathbf{k}'' = k_0 \nabla S$, it can be written as^{37,38}

$$D(\mathbf{x}, \mathbf{k}', \omega) = (k')^2 - \left(\frac{\omega}{c}\right)^2 [N(\mathbf{x}, \mathbf{k}', \omega)^2 + (\nabla I)^2]. \quad (10)$$

The imaginary part of the eikonal equation, $\mathbf{v}_g \cdot \nabla I = 0$, simply states that the intensity of the beam is constant along each ray path. For high frequency electromagnetic waves, the ion dynamics can be neglected and the refractive index can be expressed, in the cold plasma approximation, by the Appleton–Hartree expression.³⁹ The term $(\nabla I)^2$ introduces a dependence of the dispersion relation on the toroidal coordinate, even in axisymmetric configurations, so that the toroidal component of the wave vector, k_ϕ , is no longer a constant. On the initial wave front the term $(\nabla I)^2$ is determined analytically. On successive wave fronts the propagation of the beam is guided by the central ray, the only ray for which the imaginary part is zero, and the term $(\nabla I)^2$ and its derivatives are calculated along the beam trajectory following the

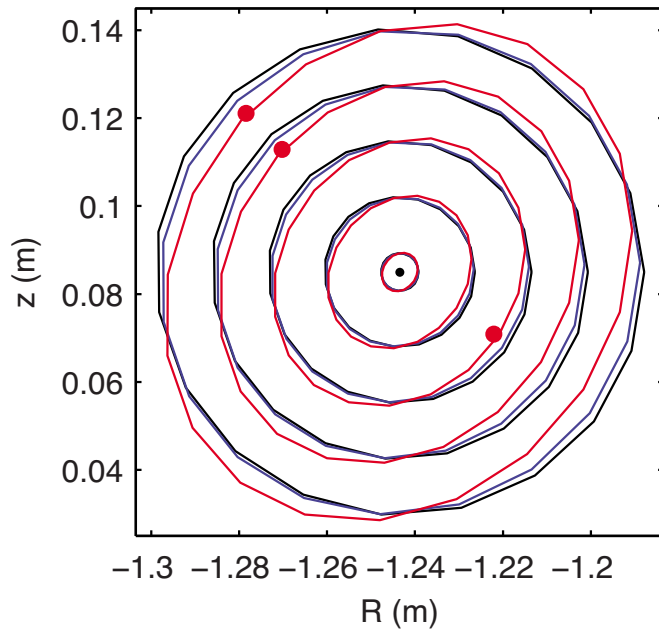


FIG. 6. (Color online) Wave front at the center of the scattering volume and at 96 cm downstream the direction of propagation (dots), compared with the initial Gaussian wave front (black). The positions of the wave fronts along the probe beam are indicated in Fig. 1.

method proposed by Nowak.³⁸ Details of the procedure are not repeated herein.

Because of the high frequency of the beam, the spreading is small and the wave front at the location of scattering can be still assumed of Gaussian form, as shown in Fig. 6, where the wave fronts at the scattering location and approximately 96 cm downstream are compared with the circular, initial wave front. This eases the computation of the Fourier spectra because the intensity profile of the beam can be calculated analytically. The relative variation of k_i measured inside the scattering volume, with respect to the central ray, is about 5×10^{-5} ; the variation in the components of \mathbf{k}_i along z and along R are instead, respectively, 1% and 50%. A consequence is that the error made in the estimate of the measured wavenumber is negligible when calculated from the central rays and using the full beam, while the width of the measured fluctuation spectrum depends on the geometry and it differs from the estimated $2a^{-1}$, as discussed in the following section.

B. Selection of wavenumbers

The ray tracing equations are solved for the injected beam and also for a single ray that initiates from the center of each detector and whose direction is determined by the orientation and the center of curvature of the collecting mirror (see Fig. 1). The position of the scattering volume is found at the geometrical intersection of incident and scattered beams. First, we find on the equatorial plane the distance of minimum approach between the central rays, which provides a guessing value for the scattering angle and for the toroidal location of scattering, which is used to select a portion of the incident beam of length $2a(\sin \theta_s)^{-1}$ (see Fig. 7).

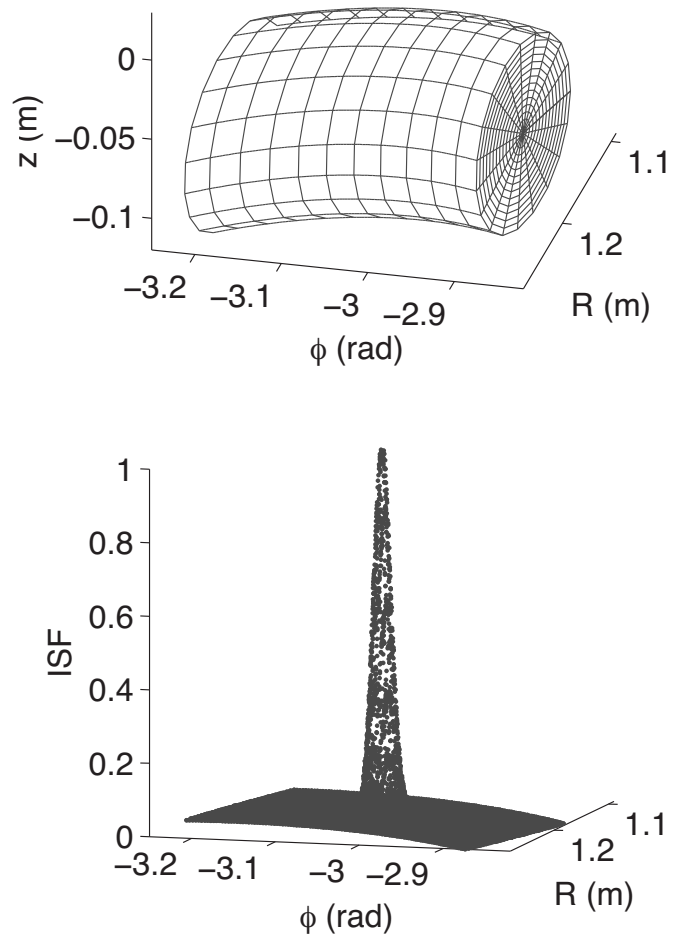


FIG. 7. Portion of the incident beam used for the computation of the ISF, with a toroidal extension of about 47 cm (a) and ISF (b), in the case of the detector measuring $k_{\perp} \approx 7.2 \text{ cm}^{-1}$.

Second, we calculate the reference values θ_0 and ϕ_0 to be used in Eq. (3). For each detector, the direction of scattering is kept fixed and parallel to the central, scattered ray, $\mathbf{k}_{s,0}$. The value of θ_0 is computed as the average of the angles between $\mathbf{k}_{s,0}$ and all the vectors $\{\mathbf{k}_i\}$ within a cylinder of diameter equal to the size of the exit window. To account for the amplitude profile of the beam at the scattering location, the average is weighted by a Gaussian function. Third, the instrumental selectivity function is computed from Eq. (3) inside the overlapping volume for all the rays and for all the values of $\{\mathbf{k}_i\}$ that result from the ray tracing equations. Figure 7 shows the results in the case of the detector that measures fluctuations with wavenumbers centered at $k_{\perp} \approx 7.2 \text{ cm}^{-1}$. For this wavenumber the toroidal extension of the overlapping region between the incident and the scattered beam is about 47 cm. Compared to this estimate, which would apply for isotropic turbulence, the effective scattering region is highly localized in the toroidal (2.3 cm) and in the radial (3 cm) direction, as seen in Fig. 7. Interestingly, while the length of the overlapping region varies of about 20 cm when k_{\perp} increases from 7.2 to 14.2 cm^{-1} , the instrumental selectivity function (ISF) maintains high spatial localization, with variations in the radial and toroidal width of only a few millimeters. We note that the radial footprint of the scattering region, as reconstructed herein, is smaller than the diameter

TABLE I. Values of wavenumber (units of cm^{-1}) and scattering angle (units of rad) for the three scattered beams shown in Fig. 1, computed from a fit over the ISF and as intersection of the central rays of probe and scattered beam.

Ch	k_r	Δk_r	k_θ	Δk_θ	k_\perp	Δk_\perp	θ_s	
3	7.41		2.7		7.7	0.7	0.132	Central rays
4	10.84		2.92		11.2	0.7	0.193	
5	14.12		3.75		14.6	0.7	0.251	
3	7.0	0.7	1.5	0.4	7.2	0.8	0.126	ISF
4	10.7	0.9	2.4	0.5	11.0	1.0	0.191	
5	14.1	0.8	3.2	0.5	14.5	0.9	0.251	

of the probe beam (2a); as a consequence the wavenumber width will be larger than the value of $2/a \approx 0.7 \text{ cm}^{-1}$ estimated from a Gaussian beam waist (see Table I).

There is no explicit dependence on the vertical coordinate, which is expected because the scattering geometry is mainly on the equatorial plane. Since the central rays of probe and receiving beams are not aligned though, the center of the detecting window is not aligned with the axis of the incident beam; this may affect the measured wavenumber spectrum $P(k_\theta)$. The ISF has been therefore modified to take into account the size and orientation of the exit window, which is modeled by a two-dimensional function, flat across the window extension and falling to zero close to the edge, more smoothly than a boxcar window to account for the fact that waves outside the viewing cylinder may fall within the aperture cone of the window and being detected.

It is likely that similar values of k are measured at different locations inside the overlapping volume, where the Bragg's condition is satisfied for given k_i and θ_s , although they will be detected with a different efficiency, depending on α . The ISF, which is a function of the cylindrical coordinates (R, ϕ, z) , can be used to weight the values of (k_r, k_θ) , measured at each location along the ray path and inside the overlapping volume. This allows to reconstruct the function $F(k_r, k_\theta)$, which represents the distribution of the expected wavenumbers measured by each detector. The function $F(k_r, k_\theta)$ is constructed from the ISF as follows

$$F(k_r, k_\theta) = \sum_{j,k,m} I_{\Delta r} I_{\Delta \theta} F_{j,k,m}. \quad (11)$$

Here, $I_{\Delta r}$ and $I_{\Delta \theta}$ are the discrete equivalent of the Kronecker δ function, defined as

$$I_{\Delta r, \Delta \theta} = \begin{cases} 1 & \bar{k}_{r, \theta} < k_{r, \theta} + \Delta \bar{k}_{r, \theta} \\ 0 & \text{otherwise.} \end{cases} \quad (12)$$

The indices $\{j, k\}$ identify individual rays on each wave front, from their radial and poloidal position, while m identifies the toroidal angle along each ray path. From the scattered and incident waves, the wave vector components of measured fluctuations are first computed in the cylindrical frame (R, ϕ, z) from Eq. (1), $\mathbf{k} = \mathbf{k}_s - \mathbf{k}_i$; then the components along the radial and the diamagnetic direction (k_r, k_θ) are calculated using the reconstructed magnetic equilibrium.

Figure 8 shows $F(k_r, k_\theta)$ for the three detectors and Table I lists the value of k_r and k_θ and the respective wavenumber width. While the bin width $\Delta \bar{k}_{r, \theta}$ affects the absolute amplitude for each detector, the relative efficiency between detectors, computed as the ratio of $F_{\text{tot}} = \sum_{k_r, k_\theta} F(k_r, k_\theta)$ for each detector to the detector with maximum amplitude, varies less than 1% when the bin width is varied of a factor 4. The F_{tot} gives a measure of the total power collected by a detector, based only on geometrical considerations. For the plasma parameters and the geometry of launching and injection used

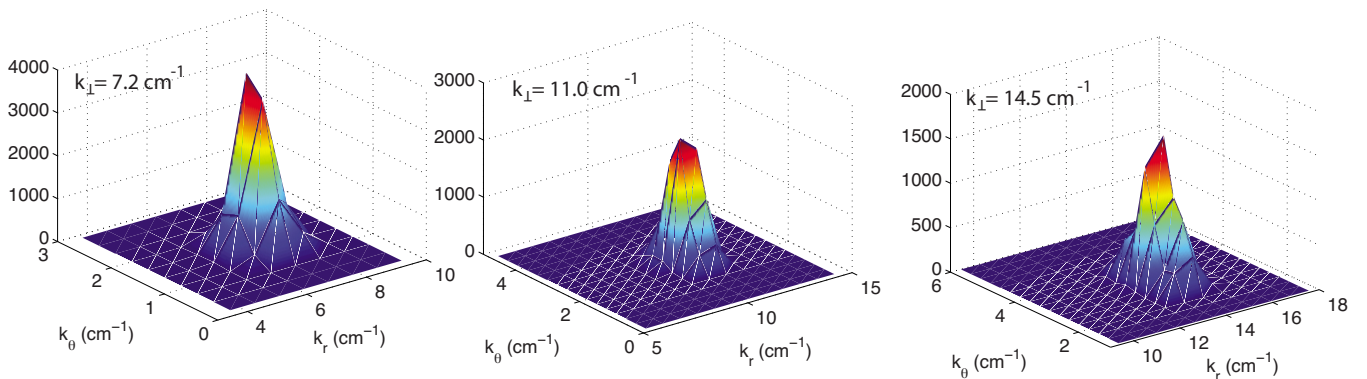


FIG. 8. (Color online) $F(k_r, k_\theta)$ computed from the ISF for the three detectors.

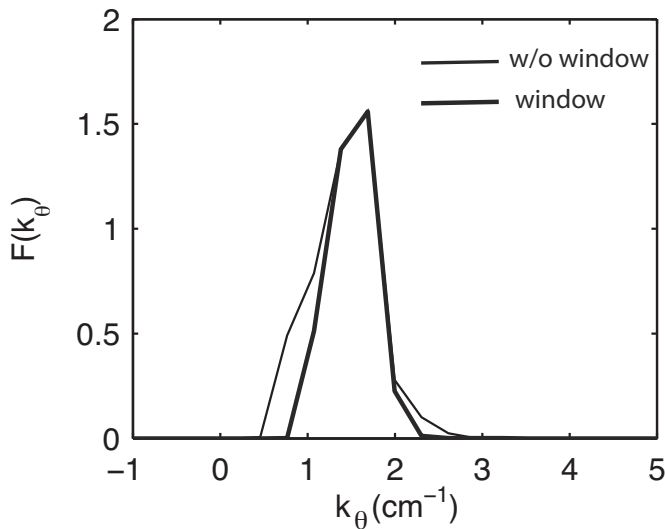


FIG. 9. $\sum_r F(k_r, k_\theta)$ for the detector measuring $k_\perp = 7.2 \text{ cm}^{-1}$. The function $F(k_r, k_\theta)$ has been normalized to its maximum before performing the sum. The thin curve is the result without taking into account the size of the exit window in the ISF, while the thick curve includes the size of the exit window.

in this work, the collection efficiency of $k_\perp = 11 \text{ cm}^{-1}$ and $k_\perp = 14.5 \text{ cm}^{-1}$ is, respectively, 87% and 67% with respect to $k_\perp = 7.2 \text{ cm}^{-1}$. The effect of including the size of the exit window in the computation of the ISF is shown in Fig. 9; it affects the extrema of the k_θ spectrum. The histograms shown in Fig. 8 have been computed over the same grid $(\bar{k}_r, \bar{k}_\theta)$ used for the computation of the wavenumber spectra from simulations. This allows to use $F(k_r, k_\theta)$, normalized to its maximum, as a mask for the simulated $P(k_r, k_\theta)$ spectra. For each detector, the resulting spectrum is then integrated over (k_r, k_θ) and corrected for the reduced efficiency. A consequence of the different detection efficiency is that it provides an artificial slope in the spectra, which is not included in the absolute calibration of the detectors and that should be taken into account also in the measured spectra. For the geometry of injection and detection considered in this work, the relative P_{tot} follows a power law $k_\perp^{(-0.59 \pm 0.06)}$; this factor flattens the measured spectra, whose spectral index β should therefore be corrected from 4.23 to 3.64.

C. Computation of spectra from simulations

Density fluctuations are computed over 64 poloidal planes, toroidally separated about 10 cm in the outboard region; this is longer than the toroidal extension of the scattering volume, which is comparable to twice the beam waist. Since along the magnetic field the wavelength is much longer than across the magnetic field, within the domain of integration of Eq. (6) fluctuations can be assumed to be constant along the toroidal direction and an integration over adjacent planes is not required. Wavenumber and frequency spectra can be computed independently over individual poloidal planes on parallel processors to decrease execution time. They will be averaged out only at a successive stage for better statistical significance and to reduce the fluctuation noise level.

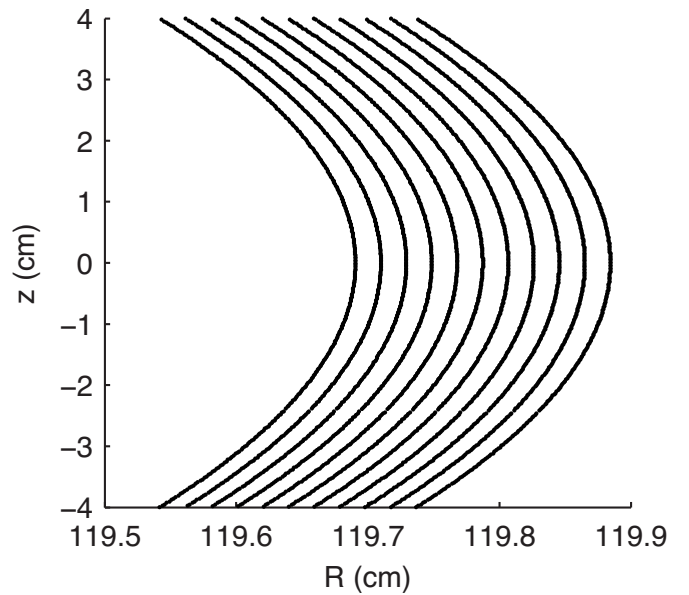


FIG. 10. Excerpt of the spatial grid used in GTS simulations, showing the flux surfaces in a limited radial region around the strip where streamers are localized.

For each poloidal plane, the computation of wavenumber and frequency spectra is performed over three successive steps, using only one dimensional fast Fourier transforms and one dimensional interpolations. The simulation grid is highly dense along the diamagnetic direction (see Fig. 10), which represents the natural direction of propagation of drift wave perturbations. Since the number of grid points changes over adjacent flux surfaces, each surface must be analyzed separately. The first step, the computation of the Fourier components along θ , $\tilde{n}(r, k_\theta, t)$, involves $N_t \times N_\psi$ operations, where N_t and N_ψ are, respectively, the number of time steps and of flux surfaces. Since the arc length along the diamagnetic direction is not constant in real coordinates (R, z) , an interpolation along each flux surface is required before computation of the Fourier transform. A new “rectified” trajectory ℓ is constructed along the diamagnetic direction using the existing grid, where the distance between neighbor points is approximated with the geometrical distance $d\ell_j = \sqrt{(R_{j+1} - R_j)^2 + (z_{j+1} - z_j)^2}$. Density fluctuations are then interpolated onto a new grid, with a coarser, uniform step, which is the same for each flux surface, to guarantee that the Nyquist value of the poloidal wavenumber is the same for all flux surfaces. After interpolation and before computation of the Fourier Transforms, density fluctuations are multiplied by the intensity profile of the beam, previously interpolated over the simulation grid.

Having selected the radial and the diamagnetic direction as our orthogonal reference system, the dependence of the poloidal wavenumber component on R is eliminated. Fourier components $\tilde{n}(r, k_\theta, t)$ are only a function of the distance between flux surfaces, which, at midplane, is given. Since the radial step at midplane is not uniform, an interpolation of the amplitude and phase of $\tilde{n}(r, k_\theta, t)$ for each value of k_θ would be required before computing the k_r components. In addition to multiply by three the number of operations, this interpo-

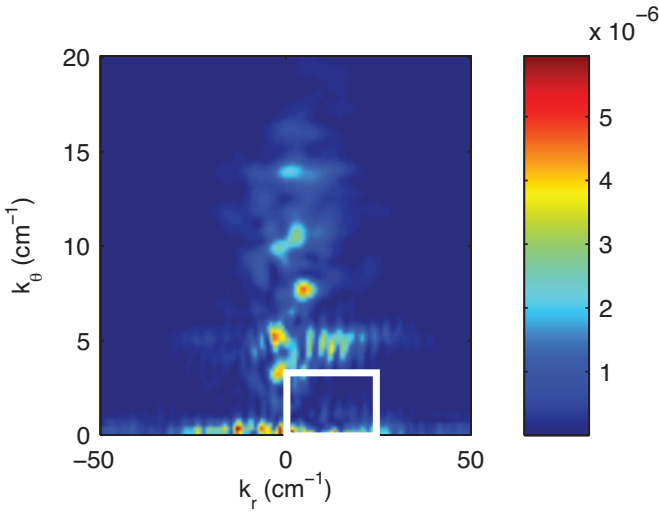


FIG. 11. (Color) Wavenumber spectrum of normalized density fluctuations \bar{n}/n_0 , weighted by the beam intensity profile and averaged over the nonlinear phase.

lation introduces errors at the boundaries of large-scale coherent structures, where the phase shift may change from a constant, spatially defined value, to a value that is associated to incoherent fluctuations and oscillates between $\pm\pi$. This effect is shown in Fig. 11: the apparent structure in k_r at $k_\theta \approx 5 \text{ cm}^{-1}$ is mostly due to jumps in the phase shift along the radial direction. Although this effect can be reduced by averaging spectra over planes, a better procedure is to preprocess density fluctuations in flux coordinates and interpolate them onto a new grid $(\hat{\psi}, \hat{\theta})$. The separation between the new flux surfaces $\Delta\hat{\psi}$ is chosen to generate in real space a uniform radial grid at midplane. The new poloidal grid is arbitrary and it is constructed using a step coarser than the original one, yet dense enough over each flux surface to minimize errors in the construction of ℓ from the curved, diamagnetic path. If the Fourier Transform along θ has been computed using the same number of points over each flux surface, the computation of $\bar{n}(k_r, k_\theta, t)$ is a straightforward operation, performed for each value of k_θ and for each time step.

The total number of operations required to compute the wavenumber spectra depends on the spatial grid, which affects the Nyquist wavenumber, and on the number of points used for the computation of the Fourier transform, which affects the wavenumber resolution. Efficiency can be increased by interpolating data onto a coarser grid, taking care that the resolution in space is sufficient to resolve the smallest scales of interest. The computation of frequency spectra is the last of the three Fourier operations. The Fourier components $\bar{n}(k_r, k_\theta, t)$ are first filtered through the ISF for all the detectors, to extract the measured (k_r, k_θ) and then integrated over wavenumbers

$$\bar{n}_S^j(k_\perp, t) = \sum_{k_r, k_\theta} \bar{n}(k_r, k_\theta, t) F_j(k_r, k_\theta) \quad j = 1, \dots, 5. \quad (13)$$

Here $\bar{n}_S^j(k_\perp, t)$ are the *synthetic density fluctuations*, i.e., the time series of density fluctuations associated with selected perpendicular wavenumbers, measured at the location of in-

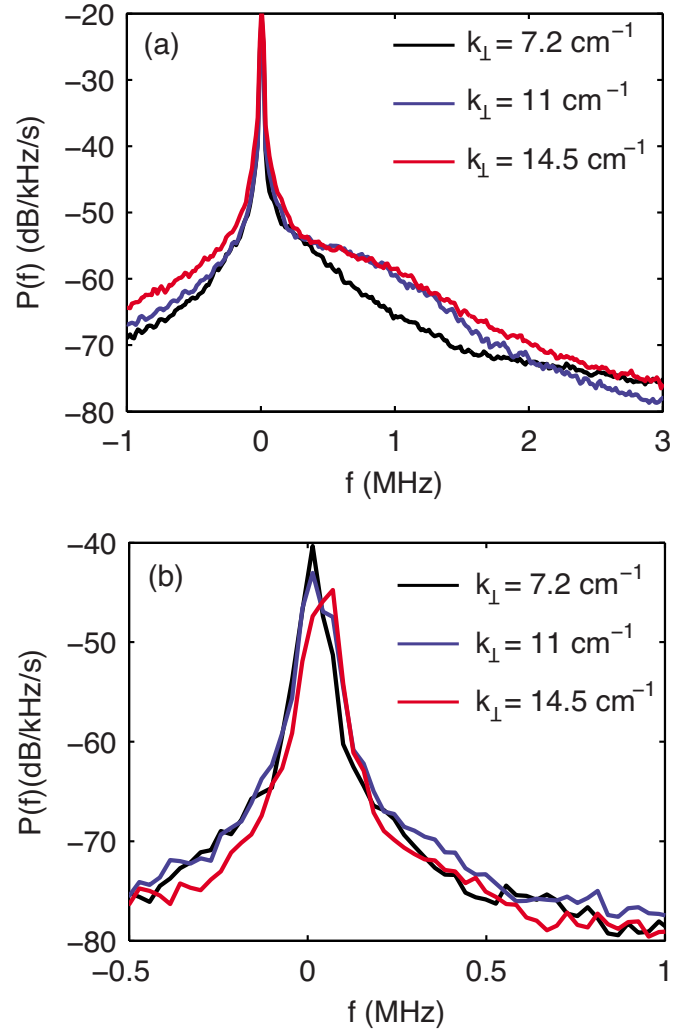


FIG. 12. (Color online) (a) Frequency spectra from the high- k scattering for $k_\perp = 7.2 \text{ cm}^{-1}$, $k_\perp = 11 \text{ cm}^{-1}$, and $k_\perp = 14.5 \text{ cm}^{-1}$. (b) Frequency spectra from simulations, for the same values of k_\perp , averaged over planes.

dividual detectors. They represent the simulation equivalent of the measured density fluctuations. The frequency spectra for the three channels, computed from $\bar{n}_S^j(k_\perp, t)$, are compared in Fig. 12. Measured spectra (a) broaden with increasing wavenumber and have maximum amplitude just below 1 MHz. Conversely, simulated spectra (b) are much narrower, although a slight widening is visible between the lowest k_\perp and the other two wavenumbers. The peaking frequency in the simulated spectra should be corrected for a Doppler shift component induced by the background $\mathbf{E} \times \mathbf{B}$ flow, which, for this experiment, is approximately 0.5 MHz toward higher frequencies for the component at the highest wavenumber. It is noteworthy that frequency peak with a proper $\mathbf{E} \times \mathbf{B}$ Doppler shift can be used to identify the measured fluctuations against theoretical predictions.⁴⁰

The discrepancy in the broadening of the spectrum could be due, for example, to a different evolutionary stage. Measured turbulence is usually in an advanced, saturated state, where the dominant instability has had enough time to saturate and interact with other modes. The resulting spectra are naturally broad, but in most cases still centered at the frequency value of the underlying instability. On the other hand,

numerical simulations usually begin at the linear stage of instabilities and end not very long after the postnonlinear saturation phase. Thus, they usually exhibit narrower spectra. It should also be noted that the center of the scattering volume illuminates the inner annulus of structures, which are likely in an earlier evolutionary stage compared to the large annulus at $R=1.20$ m. When computed at this latter location, the frequency spectra appear slightly broader.

IV. SYSTEMATIC ERRORS IN THE COMPUTATION OF SYNTHETIC SPECTRA

There are different sources of uncertainties and systematic errors in the computation of synthetic spectra. They may arise from errors in the measured profiles, in the integration of measured profiles onto magnetic coordinates, or from an imperfect mapping of magnetic topology to laboratory coordinates. All of them affect the results of ray tracing equations and thus the predicted position of the scattering volume and the wavenumbers estimated from the intersection of incident and scattered beams.

The more significant errors are those associated with the extension of the scattering volume and with the total simulation runtime. The latter affects the spectra in two ways: the minimum frequency that can be resolved and, more important, the value of the spectral index. The slope of wavenumber spectra, and therefore the spectral index value, depends in fact on the evolutionary stage of turbulence. A transfer of energy from small to large scales is observed in the GTS simulations during the nonlinear phase and spectra progressively peak at smaller values of $|k_\theta|$,¹⁵ as Fig. 13 shows. Here we plot the k_r and k_θ integrated from $P(k_r, k_\theta)$ during three time slices during the nonlinear phase.

Figure 14(a) shows the evolution of the spectral index during the nonlinear phase, extracted from the synthetic $P(k_\perp)$ spectra during 17 time windows of duration $0.4 \mu\text{s}$ each. The spectral index increases in absolute value during the nonlinear phase from $\beta \approx 1.1$ to $\beta \approx 2.7$. The steepening of the spectra is mostly due to an increase in power in the range of small perpendicular wavenumbers, as shown in Fig. 14(b), where the evolution of $P(k_\perp)$ is plotted for the three channels. If spectra are computed before a stationary phase is reached, the spectral index will be systematically lower in absolute value. Herein the need for running simulations for a time sufficiently long that the scaling in the inertial range is statistically robust.

The position of the scattering volume has no significant effect on the synthetic $P(k_\perp)$, at least for this simulation run. When computed over a region centered on the streamers at $R=1.20$ m (i.e., a beam waist distance from the real center of scattering), differences in the value of $P(k_\perp)$ vary from 3% to 6% between the smallest and the largest wavenumber. This is due to the fact that the high- k scattering measures values of k_\perp much smaller than those at which simulated spectra peak, as shown in the inset in Fig. 11. Fluctuations at scales comparable or larger than the inverse beam waist $\pi/a \approx 1 \text{ cm}^{-1}$ are strongly reduced in amplitude by the Gaussian windowing. Differences in the wavenumber spectra in this range are therefore negligible. Since errors in the po-

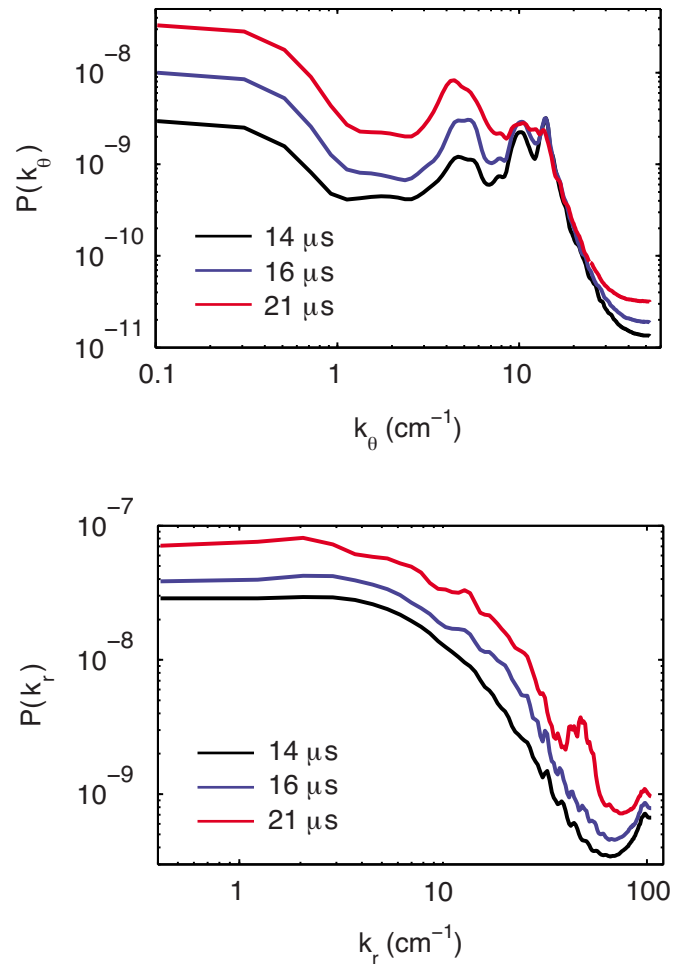


FIG. 13. (Color online) Integrated wavenumber spectra during the nonlinear phase, averaged over 64 planes. (a) $P(k_\theta) = \sum_{k_r} P(k_r, k_\theta)$, normalized to the total k_r range, $\Delta k_r = 104.7 \text{ cm}^{-1}$; (b) $P(k_r) = \sum_{k_\theta} P(k_r, k_\theta)$, normalized to the total k_θ range in simulations, $\Delta k_\theta = 52.4 \text{ cm}^{-1}$.

sition of the scattering volume given by imperfect magnetic mapping or experimental uncertainties will be likely smaller than the beam waist, the consequent uncertainties in the final spectra are negligible.

While the position of the scattering volume does not significantly affect the synthetic spectra, differences can be remarkably large if the illumination profile of the beam is not correctly taken into account, as shown in Fig. 14(c). Here the spectra have been computed over half cross-section, on the low field side, but the ISF has been used to extract the synthetic power for the three detectors. Compared to (b), where the spectra have been computed over the scattering volume, the wavenumber spectra do not follow a power law, and the power associated with the central detector is higher than that associated with the other two. This is due to the fact that large scale fluctuations, not reduced by the Gaussian amplitude of the beam, are resolved by the Fourier analysis and affect the final spectrum at the lowest wavenumber values. Interestingly, frequency spectra for these simulations are minimal affected by the size of the scattering volume.

Another important source of error arises when neglecting the ISF. As discussed in Sec. III B, the detection efficiency decreases with increasing wavenumber, i.e., for in-

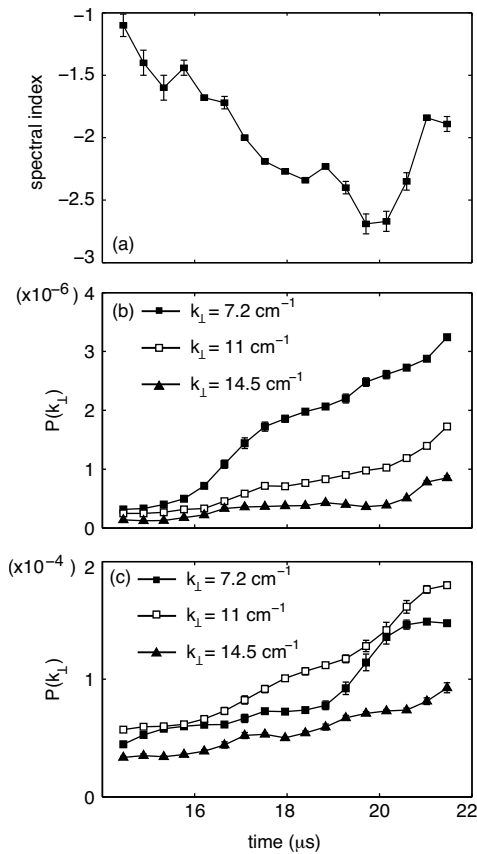


FIG. 14. (Color online) (a) Evolution of the spectral index during the non-linear phase, computed over time windows of $0.4 \mu\text{s}$. (b) Evolution of $P(k_{\perp})$ for wavenumbers $k_{\perp}=7.2 \text{ cm}^{-1}$ (black squares), $k_{\perp}=11 \text{ cm}^{-1}$ (white squares), $k_{\perp}=14.5 \text{ cm}^{-1}$ (triangles).

creasing scattering angle with respect to the direction of injection. The relative F_{tot} for different detectors should therefore be taken into account when filtering the spectra from simulations. Two cases are compared in Fig. 15: in the

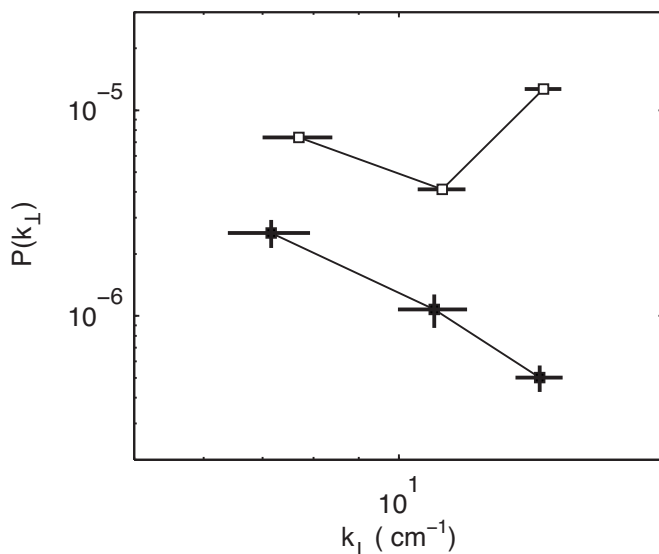


FIG. 15. Synthetic spectra computed without taking into account the ISF (open squares) and with the ISF (black squares). In the latter case the spectral index is $\beta=(2.28 \pm 0.04)$.

first case wavenumbers are selected from the results of ray tracing equations, as the values given by the intersection between central rays (see Table I). Spectra $P(k_{\perp})$ are then computed as the integrated power spectrum in the range of (k_r, k_{θ}) with half width $\Delta k=2/a \approx 0.7$. In the second case, the wavenumber spectra are multiplied by $F(k_r, k_{\theta})$ and normalized by the ratio of $F(k_r, k_{\theta})$ for the different channels. In both cases, spectra have been computed during a time window of $4 \mu\text{s}$, having discarded the first half of the time series. The spectral index, estimated from the synthetic spectra is (2.28 ± 0.04) , yet lower in absolute value than the measured 3.64.

V. CONCLUSIONS

The comparison between density fluctuations from global, nonlinear, gyrokinetic simulations and those measured by coherent scattering experiments is affected by a number of systematic errors. The largest sources of uncertainty come from the localization of scattering measurements, from the simulation runtime and from the different wavenumber range covered. The growth rate of ETG instabilities is high and measured turbulence is expected to be in a fully saturated state, with spectral slope well defined in the inertial range. Simulations should be run for a time sufficiently long to guarantee saturation of spectra, otherwise the calculated spectral index could be significantly different. Simulated spectra cover almost three orders of magnitude in (k_r, k_{θ}) , while scattering measurements are local in space and over a limited range of perpendicular wavenumbers, a subset of the full (k_r, k_{θ}) space covered by simulations. The spectral index will be inevitably different. Simulated spectra peak at values of poloidal wavenumbers much higher than those measured by the high- k scattering diagnostic. It is possible that the measured spectrum is not representative of the ETG turbulence and that, with the present experimental configuration, it would be difficult to validate numerical codes against experiments only based on the slope of the wavenumber spectrum.

When simulated spectra are filtered through the ISF and the finite extension of the scattering volume is taken into account, a closer agreement is found between measurements and simulations. An important issue for code and data validation arises from the combined effect of the finite extension of the region of scattering and the low value of k_{θ} measured with the present layout, together with the dependence of the detection efficiency on the scattering angle. The first two result in a power law dependence of the spectra also in cases where spectra are not sloped, the second causes a steepening of simulated wavenumber spectra and a flattening of measured spectra. These two effects could explain why, for example, the same spectral index was measured both in the case of inboard and outboard measurements, despite of the electron temperature being so different.¹¹ It is noteworthy that the measured frequency spectra for the two injection configurations looked instead well distinct, suggesting that frequency spectra might be more representative than wavenumber spectra for theoretical model validations. All these

issues should be explored over other theoretical models and simulations, run for different experimental configurations.

ACKNOWLEDGMENTS

S. Nowak is acknowledged for help on the computation of the complex eikonal. H. Park and Y. Ren are acknowledged for fruitful discussion on the high- k scattering diagnostic. This work is supported by U.S. DOE under Contract No. DE-AC02-09-CH11466 and by the SciDAC GPS-TTBP project. This research used resources of the Oak Ridge Leadership Facility at the Oak Ridge National Laboratory, which is supported by the Office of Science of the U.S. Department of Energy under Contract No. DE-AC05-00OR22725. The computer time was granted as part of the DOE Innovative and Novel Computational Impact on Theory and Experiment (INCITE) program. F. M. Poli is supported by the UK EPSRC.

- ¹M. Ono, S. M. Kaye, Y.-K. M. Peng, G. Barnes, W. Blanchard, M. D. Carter, J. Chrzanowski, L. Dudek, R. Ewig, D. Gates, R. E. Hatcher, T. Jarboe, S. C. Jardin, D. Johnson, R. Kaita, M. Kalish, C. E. Kessel, H. W. Kugel, R. Maingi, R. Majeski, J. Manickam, B. McCormack, J. Menard, D. Mueller, B. A. Nelson, B. E. Nelson, C. Neumeyer, G. Oliaro, F. Paoletti, R. Parsells, E. Perry, N. Pomphrey, S. Ramakrishnan, R. Raman, G. Rewoldt, J. Robinson, A. L. Roquemore, P. Ryan, S. Sabbagh, D. Swain, E. J. Synakowski, M. Viola, M. Williams, J. R. Wilson, and NSTX Team, *Nucl. Fusion* **40**, 557 (2000).
- ²H. Bigrari, P. H. Diamond, and P. Terry, *Phys. Fluids B* **2**, 1 (1990).
- ³R. E. Waltz, G. D. Kerbel, and J. Milovich, *Phys. Plasmas* **1**, 2229 (1994).
- ⁴T. S. Hahm and K. H. Burrell, *Phys. Plasmas* **2**, 1648 (1995).
- ⁵R. J. Maqueda, G. A. Wurden, D. P. Stotler, S. J. Zweben, B. LaBombard, J. L. Terry, J. L. Lowrance, V. J. Mastrocola, G. F. Renda, D. A. D'Ippolito, J. R. Myra, and N. Nishino, *Rev. Sci. Instrum.* **74**, 2020 (2003).
- ⁶E. Mazzucato, *Phys. Plasmas* **10**, 753 (2003).
- ⁷C. Fenzi, R. J. Fonck, M. Jakubowski, and G. R. McKee, *Rev. Sci. Instrum.* **72**, 988 (2001).
- ⁸G. R. McKee, C. Fenzi, R. J. Fonck, and M. Jakubowski, *Rev. Sci. Instrum.* **74**, 2014 (2003).
- ⁹S. Coda, M. Porkolab, and T. N. Carlstrom, *Rev. Sci. Instrum.* **63**, 4974 (1992).
- ¹⁰E. Mazzucato, D. R. Smith, R. E. Bell, S. M. Kaye, J. C. Hosea, B. P. LeBlanc, J. R. Wilson, P. M. Ryan, C. W. Domier, N. C. Luhmann, H. Yuh, W. Lee, and H. Park, *Phys. Rev. Lett.* **101**, 075001 (2008).
- ¹¹E. Mazzucato, R. E. Bell, S. Ethier, J. C. Hosea, S. M. Kaye, B. P. LeBlanc, W. W. Lee, P. M. Ryan, D. R. Smith, W. X. Wang, J. R. Wilson, and H. Yuh, *Nucl. Fusion* **49**, 055001 (2009).
- ¹²D. R. Smith, S. M. Kaye, W. Lee, E. Mazzucato, H. K. Park, R. E. Bell, C. W. Domier, B. P. LeBlanc, F. M. Levinton, N. C. Luhmann, Jr., J. E. Menard, and H. Yuh, *Phys. Rev. Lett.* **102**, 225005 (2009).
- ¹³D. R. Smith, S. M. Kaye, W. Lee, E. Mazzucato, H. K. Park, R. E. Bell, C. W. Domier, B. P. LeBlanc, F. M. Levinton, N. C. Luhmann, Jr., J. E. Menard, and H. Yuh, *Phys. Plasmas* **16**, 112507 (2009).
- ¹⁴W. X. Wang, Z. Lin, W. M. Tang, W. W. Lee, S. Ethier, J. L. V. Lewandowski, G. Rewoldt, T. S. Hahm, and J. Manickam, *Phys. Plasmas* **13**, 092505 (2006).
- ¹⁵S. Ethier, W. X. Wang, T. S. Hahm, S. M. Kaye, W. W. Lee, E. Mazzucato, G. Rewoldt, W. M. Tang, and F. Poli, Proceedings of the 51st APS-DPP Annual Meeting, Atlanta, Georgia, 2009, Vol. 54.
- ¹⁶P. W. Terry, M. Greenwald, J.-N. Leboeuf, G. R. McKee, D. R. Mikkelsen, W. M. Nevins, D. E. Newman, and D. P. Stotler, *Phys. Plasmas* **15**, 062503 (2008).
- ¹⁷M. Greenwald, *Phys. Plasmas* **17**, 058101 (2010).
- ¹⁸R. V. Bravenec and W. M. Nevins, *Rev. Sci. Instrum.* **77**, 015101 (2006).
- ¹⁹C. Holland, A. E. White, G. R. McKee, M. W. Shafer, J. Candy, R. E. Waltz, L. Schmitz, and G. R. Tynan, *Phys. Plasmas* **16**, 052301 (2009).
- ²⁰P. Devynck, X. Garbet, C. Laviron, J. Payan, S. K. Saha, F. Gervais, P. Hennequin, A. Quémeœur, and A. Truc, *Plasma Phys. Controlled Fusion* **35**, 63 (1993).
- ²¹E. Mazzucato, *Plasma Phys. Controlled Fusion* **48**, 1749 (2006).
- ²²D. R. Smith, E. Mazzucato, T. Munsat, H. Park, D. Johnson, L. Lin, C. W. Domier, M. Johnson, and N. C. Luhmann, *Rev. Sci. Instrum.* **75**, 3840 (2004).
- ²³D. R. Smith, E. Mazzucato, T. Munsat, H. Park, D. Johnson, L. Lin, C. W. Domier, M. Johnson, and N. C. Luhmann, *Rev. Sci. Instrum.* **79**, 123501 (2008).
- ²⁴D. R. Smith, "Investigation of electron gyroscale fluctuations in the National Spherical Torus Experiment," Ph.D. thesis, Princeton University, 2009.
- ²⁵F. Jenko, W. Dorland, and G. W. Hammett, *Phys. Plasmas* **8**, 4096 (2001).
- ²⁶F. Romanelli, *Phys. Fluids B* **1**, 1018 (1989).
- ²⁷T. S. Hahm and W. M. Tang, *Phys. Fluids B* **1**, 1185 (1989).
- ²⁸W. Dorland, F. Jenko, M. Kotschenreuther, and B. N. Rogers, *Phys. Rev. Lett.* **85**, 5579 (2000).
- ²⁹J. Candy, R. E. Waltz, M. R. Fahey, and C. Holland, *J. Phys.: Conf. Ser.* **78**, 012008 (2007).
- ³⁰Z. Lin, I. Holod, L. Chen, P. H. Diamond, T. S. Hahm, and S. Ethier, *Phys. Rev. Lett.* **99**, 265003 (2007).
- ³¹Y. Idomura, S. Tokuda, and Y. Kishimoto, *Nucl. Fusion* **43**, 234 (2003).
- ³²A. Bottino, A. Peeters, R. Hatzky, S. Jolliet, B. McMillan, T. Tran, and L. Villard, *Phys. Plasmas* **14**, 010701 (2007).
- ³³J. Delucia, S. C. Jardin, and A. M. M. Todd, *J. Comput. Phys.* **37**, 183 (1980).
- ³⁴I. H. Hutchinson, *Principles of Plasma Diagnostics*, 2nd ed. (Cambridge University Press, Cambridge, 2002), pp. 293–296.
- ³⁵S. Choudhary and L. B. Felsen, *IEEE Trans. Antennas Propag.* **21**, 827 (1973).
- ³⁶S. Weinberg, *Phys. Rev.* **126**, 1899 (1962).
- ³⁷E. Mazzucato, *Phys. Fluids B* **1**, 1855 (1989).
- ³⁸S. Nowak and A. Orefice, *Phys. Plasmas* **1**, 1242 (1994).
- ³⁹T. H. Stix, *Waves in Plasmas* (Springer-Verlag, New York, 1992), pp. 37–40.
- ⁴⁰K. L. Wong, N. L. Bretz, T. S. Hahm, and E. Synakowski, *Phys. Lett. A* **236**, 339 (1997).